

Solution Structure and Backbone Dynamics of the TGF β Type II Receptor Extracellular Domain^{†,‡}

Shashank Deep,[§] Kerfoot P. Walker, III,[§] Zhanyong Shu,^{||} and Andrew P. Hinck^{*,§}

Department of Biochemistry and Institute of Biotechnology, University of Texas Health Science Center at San Antonio, San Antonio, Texas 78229-3900

Received March 6, 2003; Revised Manuscript Received June 18, 2003

ABSTRACT: Isoforms of transforming growth factor β (TGF β) are 25 kDa homodimeric polypeptides that signal by binding and bringing together two related, functionally distinct cell surface receptors designated as T β R1 and T β R2. Here, we report the solution structure of the 13.8 kDa extracellular domain of human T β R2 (ecT β R2) as calculated from N^N–H^N, C ^{α} –H ^{α} , and C ^{α} –C^O residual dipolar coupling restraints in conjunction with NOE distance, dihedral angle, and scalar coupling restraints. Comparison of the free ecT β R2 solution structure with the TGF β 3-bound ecT β R2 crystal structure reveals backbone conformations that superimpose with RMSDs of 1.0 Å over the regions of regular secondary structure and 1.4 Å overall. The differences in structure fall mainly in loop regions that are either poorly defined by the available NMR data or are involved in crystal contacts. The noted similarities between the NMR structure of the free form and the crystal structure of the TGF β -bound form are also consistent with the close correspondence, 0.16 Å RMSD for regions of secondary structure and 0.51 Å RMSD overall, for the crystal structure of free ecT β R2 as compared to the crystal structure of TGF β 3-bound ecT β R2. Despite the apparent similarities between the free and the bound forms, there appears to be small but significant differences in structure involving the interfacial contact region of the receptor. Measurements of backbone ¹⁵N relaxation times and interpretation of these by the model-free formalism with axial diffusional anisotropy further reveal significant ms to μ s time scale motions centered about two of the conserved disulfide bonds and in several residues that comprise the TGF β binding surface. Together, these observations indicate that binding likely occurs through a mechanism with a small component of induced fit character, whereby flexibility within the receptor facilitates the transition to the TGF β -bound state.

The three major isoforms of transforming growth factor β , TGF β 1,¹ TGF β 2, and TGF β 3, along with other structurally related polypeptides of the TGF β family such as activins and bone morphogenic proteins (BMPs) are 25 kDa disulfide linked homodimers that play crucial roles in regulating cellular homeostasis and in controlling cell fate (1, 2). Polypeptides of the TGF β family signal by binding and bringing together in a tetrameric complex the small extracellular domains of two related, functionally distinct single-pass transmembrane receptor kinases, known as the type I

and II receptors (3, 4). The signal is transduced through a phosphorylation cascade (5), wherein the type II receptor phosphorylates the type I receptor, which in turn phosphorylates the cytoplasmic effectors of the pathway, known as SMADs (6).

TGF β isoforms function to block the cell cycle transition from G1 to S (1), and thus function as potent growth inhibitors, with important roles in tumor suppression (7). Other biological activities induced by TGF β isoforms include immune suppression, induction of angiogenesis, maintenance of the extracellular matrix, and regulation of cellular motility (1). Misregulation, or alterations in these responses through defects in protein components of the TGF β pathway, has been implicated in a variety of human diseases, including carcinogenesis (7, 8) and fibrosis (8, 9). It has been further shown that inhibition of the TGF β pathway has favorable effects in disease models in which TGF β has been shown to play a causative role (10–17). A deeper understanding of the ligand–receptor interactions involved in activation of the TGF β pathway may therefore assist in the development of small inhibitors that prove beneficial in treating diseases, such as cancer and fibrosis.

Chemical cross-linking studies using radiolabeled TGF β isoforms and mutant cell lines lacking T β R1 or T β R2 have shown that T β R2 binds TGF β in a T β R1-independent manner (18). T β R1 differs relative to T β R2 in that its TGF β

[†] Financial support was provided by the NIH (GM58670 and RR13879 to A.P.H.) and the Robert A. Welch Foundation (AQ1499 to A.P.H.).

[‡] The 10 lowest energy ecT β R2 structures have been deposited in the Protein Data Bank under accession code 1PLO.

* Corresponding author. Tel: (210) 567-8780. Fax: (210) 567-8778. E-mail: hinck@uthscsa.edu.

[§] Department of Biochemistry.

^{||} Institute of Biotechnology.

¹ Abbreviations: 2-D, two-dimensional; 3-D, three-dimensional; 6-O-PC, 1,2-di-*O*-hexyl-*sn*-glycero-3-phosphocholine; 14-O-PC, 1,2-di-*O*-tetradecyl-*sn*-glycero-3-phosphocholine; CPMG, Carr–Purcell–Meiboom–Gill; ecT β R2, residues 15–136 of the human transforming growth factor β type II receptor extracellular domain; FID, free induction decay; HSQC, heteronuclear single quantum correlation; NMR, nuclear magnetic resonance; NOE, nuclear Overhauser effect; RDC, residual dipolar coupling; RMSD, root-mean-square deviation; T β R2, transforming growth factor β type II receptor; T β R1, transforming growth factor β type I receptor; TGF β , transforming growth factor β .

binding properties are T β R2-dependent (18). Two possible mechanisms for assembly have been proposed based upon these observations (5). Mechanism 1 states that T β R1 binds through contacts with amino acid residues from both TGF β and T β R2, whereas mechanism 2 states that TGF β , T β R2, or both undergo a structural rearrangement upon binding, exposing a binding site to which T β R1 preferentially binds.

Structural studies conducted to date provide considerable insight as to the probable mechanism of assembly. The 2.2 Å crystal structure of the extracellular domain of human T β R2 in complex with human TGF β 3 revealed that T β R2 binds TGF β 3 by inserting a binding ridge between the exposed fingertip segments of TGF β (19). Crystal structures of the uncomplexed forms of the T β R2 extracellular domain (20) and TGF β 3 (21) have also been reported. The T β R2 extracellular domain structure was determined to 1.1 Å and was reported simultaneously with the structure of the T β R2-TGF β 3 complex. A detailed comparison of the free and TGF β 3-bound T β R2 extracellular domain structures has not been presented, although cursory inspection reveals no major differences.

The 2.0 Å crystal structure of free TGF β 3 differs relative to the T β R2-bound form in two important respects. The free structure exhibits a well-ordered three-and-a-half turn interfacial α -helix and a canonical arrangement of monomers, designated as the closed form. The bound form, in contrast, lacks sufficient electron density to permit accurate modeling the interfacial α -helix and an alternative arrangement of monomers, designated as the open form (19). CD and NMR studies indicate this structural difference does not arise as a consequence of T β R2 binding, as the uncomplexed form of TGF β 3 exhibits reduced helical content (22) and a lack of detectable secondary structure in the region corresponding to the interfacial α -helix (23, 24). The structural and biophysical information presently available thus indicates that TGF β receptor assembly occurs through a mechanism in which neither the T β R2 extracellular domain nor TGF β undergo significant structural rearrangements upon binding.

The alternative mechanism, in which the type I receptor binds through contacts with both TGF β and T β R2, is therefore currently favored. This mode of interaction is indirectly supported by a structural model of the extracellular component of the TGF β -T β R1-T β R2 complex (19), which has been developed based on crystal structures of the ecT β R2-TGF β 3 (19) and ecBMPRI1A-BMP2 complexes (25). The model positions the binding site for T β R1 adjacent to that of T β R2, such that there exists an extensive interface between the type I and the type II receptor extracellular domains that might facilitate assembly (19).

Here, we describe the 3-D solution structure of the human T β R2 extracellular domain (ecT β R2) and present a comparison of this structure to the crystal structures of free and TGF β 3-bound ecT β R2. These comparisons reveal small but significant structural changes in the TGF β binding region of the receptor. Complementary information, provided by backbone ^{15}N relaxation measurements, reveals significant ms to μs time scale motions centered about two of the conserved disulfide bonds and in several residues that comprise the TGF β binding surface. Together, these observations indicate that conformational flexibility is likely important in enabling T β R2 to engage TGF β through a mechanism with a minor component of induced fit character.

EXPERIMENTAL PROCEDURES

Sample Preparation. Samples of the human T β R2 extracellular domain, ecT β R2, uniformly labeled with ^{15}N or $^{15}\text{N},^{13}\text{C}$ were obtained by recombinant expression in *Escherichia coli* strain BL21(DE3) as previously described (26). Samples selectively labeled with ^{15}N cysteine and ^{15}N methionine were prepared similarly, with the exception that the growth medium contained unlabeled glucose, unlabeled NH_4Cl , and the appropriate ^{15}N selectively labeled amino acid at a concentration of 0.025 g L^{-1} . Samples used for NMR spectroscopy were prepared in 25 mM sodium acetate, 25 mM NaCl, 5% $^2\text{H}_2\text{O}$ at pH 5.5. Samples in 99.99% $^2\text{H}_2\text{O}$ were prepared in the same manner, except deuterated sodium acetate was used in place of unlabeled sodium acetate. NMR samples were approximately 310 μL in volume and were contained in 5 mm Shigemi microcells sealed with Teflon tape. Protein concentrations were based on the calculated molar extinction coefficient, 8000 $\text{M}^{-1} \text{cm}^{-1}$, and were 1.0 mM, unless indicated otherwise.

NMR Spectrometers. NMR measurements were made using either a Bruker AMX2 500 MHz spectrometer equipped with a 5 mm ^1H , ^{13}C , ^{15}N single axis gradient probe or a Bruker DRX 600 MHz spectrometer equipped with a 5 mm ^1H , ^{13}C , ^{15}N , ^{31}P triple axis gradient probe. The temperature was maintained at 27 °C, unless indicated otherwise.

Dihedral Angle Restraints. Backbone ϕ and ψ dihedral angle restraints for roughly one-third of the residues in the ecT β R2 domain were derived using the program TALOS (27). An error range of $\pm 35^\circ$ was assigned to each for the purpose of the structural calculations. χ_1 dihedral angle restraints for amino acid residues with side chain β -methylene protons were derived by measuring $^3J_{\text{H}\alpha-\text{H}\beta}$ and $^3J_{\text{N}-\text{H}\beta}$ scalar couplings using the 3-D H α H β (28) and 3-D HNH β (29) experiments, respectively. Restraints were derived only for those amino acids exhibiting nondegenerate β -methylene protons and were assigned values of +60, -60, or +180 degrees and an error range of $\pm 30^\circ$. Three-bond $\text{H}^{\text{N}}-\text{H}^{\alpha}$ coupling constants were determined by recording a ^{15}N -separated HNHA spectrum and by calculating the $^3J_{\text{HNH}\alpha}$ couplings from the ratio of the diagonal and cross-peak intensities, as described (30). Error estimates were obtained by substituting the RMS noise for the cross-peak intensity.

NOE Distance Restraints. NOE distance restraints were initially derived from 3-D ^{15}N - and ^{13}C -edited NOESY data sets collected using mixing times of 120 and 75 ms, respectively. Ambiguities that arose in the assignment of the 3-D ^{13}C -edited spectrum were further resolved using a 4-D ^{13}C -, ^{13}C -edited NOESY spectrum collected with a mixing time of 90 ms. Ambiguities that arose in the assignment of amide-aliphatic or amide-amide NOEs in the 3-D ^{15}N -edited spectrum were further resolved by recording 3-D ^{15}N -, ^{13}C -edited or ^{15}N -, ^{15}N -edited NOESY spectra, respectively. The mixing times used for the ^{15}N -, ^{13}C -edited and ^{15}N -, ^{15}N -edited experiments were 131 and 85 ms, respectively. The NOE intensities were converted to distance restraints using a modified form of the isolated spin-pair approximation (31, 32).

Residual Dipolar Couplings. One-bond $^1\text{H}-^{15}\text{N}$, $^1\text{H}^{\alpha}-^{13}\text{C}^{\alpha}$, and $^{13}\text{C}^{\alpha}-^{13}\text{C}^{\text{O}}$ residual dipolar coupling (RDC)

restraints were obtained by measuring the corresponding splittings for ecT β R2 tumbling isotropically or partially aligned with respect to the static field. Partial alignment was achieved using 4% (w/v) ether-based lipid bicelles, 14-OPC and 6-OPC, mixed in molar ratio of 3:1 (Avanti Polar Lipids) (33). The lipids were reconstituted in buffer consisting of 25 mM sodium acetate, 25 mM NaCl, 7% $^2\text{H}_2\text{O}$ at pH 5.5. The ^1H – ^{15}N splittings were measured using a 2.0 mM ^{15}N ecT β R2 sample, whereas the ^1H – ^{13}C and ^{13}C – ^{13}C splittings were measured using a 0.80 mM ^{13}C , ^{15}N ecT β R2 sample. Isotropic samples were prepared and treated in a manner identical to the partially oriented ones, with the exception that lipid bicelles were not included.

The $\text{N}^{\text{H}}\text{--H}^{\text{N}}$, $\text{C}^{\alpha}\text{--H}^{\alpha}$, and $\text{C}^{\alpha}\text{--C}^{\text{O}}$ splittings for both the partially oriented and the isotropic samples were measured at 40 °C. The $\text{N}^{\text{H}}\text{--H}^{\text{N}}$ and $\text{C}^{\alpha}\text{--C}^{\text{O}}$ splittings were measured using the 600 MHz spectrometer using 2-D IPAP–HSQC (34) and 3-D C^{α} -coupled HNCQ (35) sequences, respectively. The $\text{C}^{\alpha}\text{--H}^{\alpha}$ splittings were measured using the 500 MHz spectrometer and a 3-D $\text{H}\alpha$ -coupled (HA)CA(CO)-NH sequence (36). The $\text{N}^{\text{H}}\text{--H}^{\text{N}}$ splittings were measured four times, whereas the $\text{C}^{\alpha}\text{--H}^{\alpha}$ and $\text{C}^{\alpha}\text{--C}^{\text{O}}$ splittings were each measured three times.

The data were processed, and the splittings were determined by peak fitting the doublets using the nonlinear fitting routine nlinLS of the nmrPipe software package (37). The experimental dipolar couplings were obtained from the difference between the splittings measured for the partially oriented and isotropic samples. RDC tables were prepared by averaging the values for each measurement and by using the pairwise difference among these as the error. Excluded from the RDC tables were residues whose errors exceeded the mean pairwise values by a factor of 2.5 or whose ^{15}N – $\{^1\text{H}\}$ NOE values were less than 0.65.

The RDC data were analyzed to yield the molecular alignment tensor by minimizing the difference between the experimentally measured RDCs and those calculated from the crystal structures of free (20) or TGF β 3-bound ecT β R2 (19). The fitting, which yielded the Euler angles (α , β , γ), the axial component of the tensor (\mathbf{D}_a), and the rhombicity (R), was performed using the program PALES (38). Modeling of the ecT β R2 alignment tensor was based on the steric model described by Zweckstetter (38) and was also accomplished using the program PALES.

Structural Calculations. Structure calculations were performed using the distance geometry-simulated annealing protocol (39) with a variable target function in torsion-angle space (40) in the program XPLOR-NIH (41). The force constants used in the structure calculations were empirically adjusted so that the variation in the ϕ and ψ dihedral angles, $^3J_{\text{HNH}\alpha}$ couplings, and RDCs apparent among the ensemble of calculated structures approximately matched the estimated errors in the measurement of these parameters. The 10 structures chosen to represent the ensemble corresponded to the lowest energy structures achieved in the final round of refinement in which 50 structures were calculated.

Backbone ^{15}N Relaxation Parameters. Backbone amide ^{15}N T_1 , ^{15}N T_2 , and ^{15}N – $\{^1\text{H}\}$ NOE relaxation data sets were recorded in an interleaved manner at a ^{15}N frequency of 60.8 MHz using ^1H -detected pulse schemes as previously described (42). The T_1 and T_2 data sets were each collected using 32 scans and a recycle time of 1.0 s. The T_1 and T_2

data sets were each acquired using 12 delay times, which varied between 8 and 1320 ms and 8–192 ms, respectively. The NOE data were recorded using 64 scans per point and was collected by alternately applying ^1H presaturation to the amide band for each successive t_1 point. Presaturation of the amide protons for the ^{15}N – $\{^1\text{H}\}$ NOE measurements was achieved by placing the ^1H carrier in the center of the amide region and by applying a 5 kHz pulse of 120° every 30 ms for a period of 1.8 s.

The T_1 and T_2 relaxation times were obtained by fitting relative peak heights as a function of T_1 or T_2 delay time to a two parameter exponential. The errors in individual T_1 and T_2 measurements were estimated by Monte Carlo simulations (43). NOE values were obtained by taking the ratio of peak intensities from experiments performed with and without ^1H presaturation and by applying a correction to take into account the incomplete recovery of both ^{15}N and ^1H magnetization (44).

All relaxation parameters were measured twice. The duplicate T_1 and T_2 data sets were merged into a single data set by averaging each value and the corresponding Monte Carlo error estimate. NOE data were handled in a similar manner, except the pairwise difference among independent measurements was used as the error.

Modeling of the Rotational Diffusion Tensor. The rotational diffusional anisotropy of the ecT β R2 domain was modeled assuming either an axially or fully asymmetric diffusion tensor using the computational strategy described by Tjandra et al. (45, 46). The relaxation data used for the calculations consisted of experimental T_1/T_2 ratios for 63 residues. Excluded from these calculations were 23 residues identified using the criteria described by Barbato et al. as undergoing high amplitude internal motion on the ns to ps time scale or exchange (47). Amide bond vector orientations were calculated from either the 10 lowest energy NMR structures or the free ecT β R2 crystal structure.

The ecT β R2 diffusion tensor was modeled by calculating the components of the inertia tensor from the coordinates of the free ecT β R2 crystal structure. The axial ratio of the diffusion tensor was then approximated using the relation

$$\mathbf{D}_{\parallel}/\mathbf{D}_{\perp} = [0.75(2(\mathbf{I}_{\perp}/\mathbf{I}_{\parallel}) - 1)]^{1/2} \quad (1)$$

This equation applies to a perfect ellipsoid (48) and therefore only roughly approximates the extent of diffusional anisotropy based upon the inertia calculation.

Modeling of Internal Motion. The internal dynamics of ecT β R2 domain were assessed by analyzing the experimental ^{15}N relaxation parameters using the model-free formalism (49–51) and by assuming that the protein tumbles as an axially symmetric rotor. This was accomplished using the program ModelFree4 and the model selection strategy based on F statistics described by Mandel et al. (52). Five different models for internal motion were considered, S^2 (model 1); S^2 , τ_e (model 2); S^2 , R_{ex} (model 3); S^2 , τ_e , R_{ex} (model 4); and S^2 , S_f^2 , τ_e (model 5).

RESULTS

NMR Shift Assignments. The protein used for the present study, designated ecT β R2, corresponds to residues 15–136 of the mature human T β R2 extracellular domain (53). This

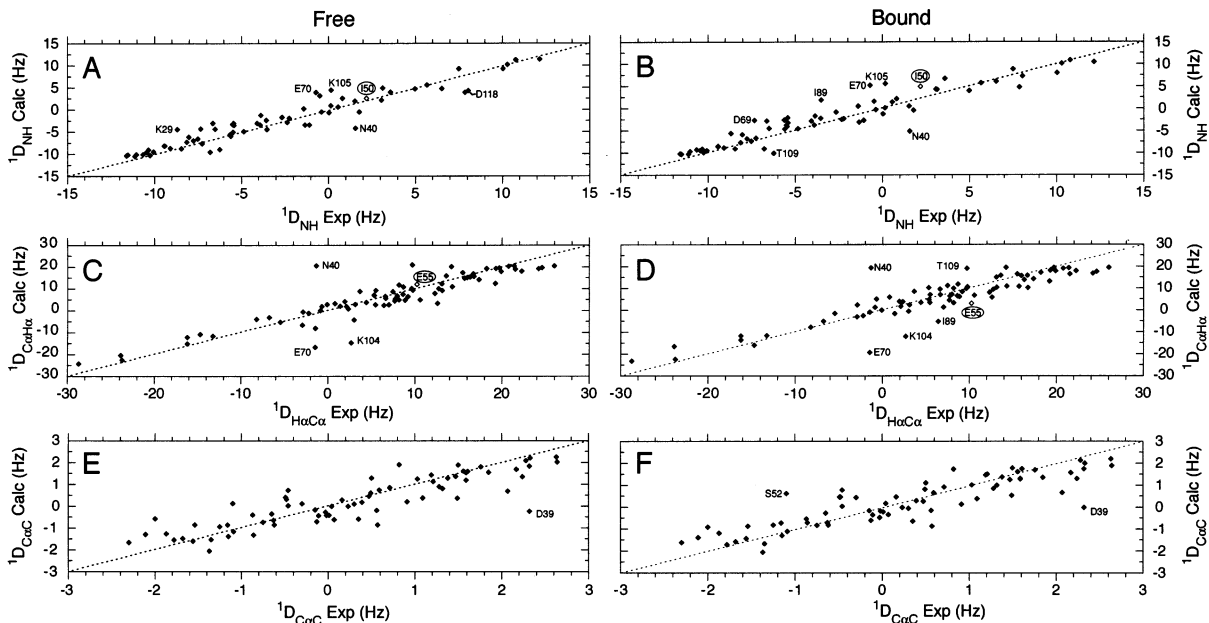


FIGURE 1: Plots of experimental vs calculated RDCs for the ecTβR2 domain. The experimental $^1D_{NH}$, $^1D_{C\alpha H\alpha}$, and $^1D_{C\alpha C}$ RDC values, shown on the ordinate in panels A and B, C and D, and E and F, respectively, were measured at 40 °C using either ^{15}N (A and B) or $^{15}N,^{13}C$ (C–F) ecTβR2 in 3:1 14-O-PC:6-O-PC bicelles (4% w/v) at pH 5.5. The calculated RDC values, shown on the abscissa, were determined using the coordinates of free (A, C, and E) or TGFβ3-bound ecTβR2 (B, D, and F), and an order tensor determined by a global fit of the $^1D_{NH}$, $^1D_{C\alpha H\alpha}$, and $^1D_{C\alpha C}$ RDC data to these same structures. The dotted line in each panel corresponds to the diagonal upon which all data points would lie if the correlations were perfect. The residue numbers indicated by black-on-white lettering identify RDC data outliers. These are defined to be any RDC whose experimental and calculated values differ by more than $2.5\times$ the mean pairwise error for their individual measurements. The residue numbers within ovals identify RDC values for I50 and E55; the significance of these are described within the text.

region includes the 12 conserved cysteine residues found among TβR2s from different species, and with the exception of 14 N-terminal residues previously shown to be dispensable for TGFβ binding (54), spans the entire predicted extracellular domain of human TβR2.

The sequential backbone and side chain 1H , ^{13}C , and ^{15}N assignments for ecTβR2 were previously reported (26). These were 92% complete and were made at pH 5.5 and 27 °C. The missing backbone and side-chain assignments of residues C78, C98-I99-M100-K101, M112-C113-S114, and I124-I125 were attributed to chemical or conformational exchange because all high-intensity correlations identified in the $^1H-^{15}N$ shift correlation spectrum of the uniformly labeled protein were assigned (26). This latter point has been confirmed in the context of the present study by preparing additional ecTβR2 samples selectively labeled with ^{15}N -Cys and ^{15}N -Met. These particular samples were prepared because among the unassigned resonances were three cysteine and two methionine residues. The analysis of these samples revealed only the cysteine and the methionine resonances that had already been assigned, thus confirming that the missing cysteine and methionine signals had not been overlooked, but as hypothesized, are broadened by either chemical or conformational exchange.

Residual Dipolar Couplings. The structure of ecTβR2 free in solution was examined by measuring backbone $^1H-^{15}N$, $^1H\alpha-^{13}C\alpha$, and $^{13}C\alpha-^{13}C^O$ RDCs of ecTβR2 dissolved in dilute liquid crystals at pH 5.5 and 40 °C. The $^1H-^{15}N$ HSQC spectra of ecTβR2 under these conditions was virtually identical to that obtained for ecTβR2 free in solution at 27 °C, indicating that neither the increased temperature nor the lipid bicelles had any significant effect on the structure. The RDC measurements were repeated three

to four times to improve the accuracy and to estimate the experimental uncertainty. This procedure yielded 68 N^H-H^N , 79 $C^\alpha-H^\alpha$, and 72 $C^\alpha-C^O$ RDCs. The mean pairwise RMSD among independent measurements was 0.92, 4.9, and 0.73 Hz for the N^H-H^N , $C^\alpha-H^\alpha$, and $C^\alpha-C^O$ RDCs, respectively.

The experimentally measured RDC values plotted versus those calculated from the free and TGFβ3-bound ecTβR2 crystal structures are shown in Figure 1 (left-handed and right-handed panels, respectively). The overall quality of the fit to the free and bound structures, as indicated by Cornilescu Q factors (55) of 0.37 and 0.41, respectively, indicate that the crystal structures provide a good description of the 3-D structure of ecTβR2 free in solution. The fact that the fits are similar is expected as the backbone atoms of the free and TGFβ3-bound ecTβR2 crystal structures superimpose with an RMSD of 0.16 Å over the regions of secondary structure and 0.51 Å overall. The parameters describing the fitted order tensors are presented in Table 1.

The fact that the two crystal structures are not identical, together with the fact that the Q factor for the free structure is slightly lower than that determined for the bound structure, has several possible interpretations. The first, which would provide the greatest insight as to the mechanism of ecTβR2-TGFβ binding, involves changes in the structure of ecTβR2 induced by TGFβ binding. Thus, as discussed below, while the experimental data indicates such structural changes do occur, these are limited and do not contribute in a significant way to the differences in the observed Q factors. The second interpretation, which is less interesting from a structure-function perspective but which as discussed below contributes more significantly to the differences in the observed Q factors, involves differences in the local geometry of exposed

Table 1: Correlation of Experimental Residual Dipolar Couplings with Corresponding Values Calculated from the Crystal Structures of Free and TGF β -Bound ecT β R2

	number of RDCs	Euler angles ^a			D_a (Hz) ^b	R^c	Q^d
		α	β	γ			
A. Free ecT β R2 Crystal Structure							
$^1D_{NH}/^1D_{CaHa}/^1D_{CaCO}$ global fit	219	72.2	141.6	62.7	6.1	0.48	0.37
$^1D_{NH}/^1D_{CaHa}/^1D_{CaCO}$ global fit ^e	211	72.7	140.9	64.8	6.3	0.48	0.26
steric model ^f		56.9	144.2	65.6	5.7	0.23	
B. TGF β -bound ecT β R2 Crystal Structure							
$^1D_{NH}/^1D_{CaHa}/^1D_{CaCO}$ global fit	219	72.2	141.3	63.5	6.0	0.51	0.41
$^1D_{NH}/^1D_{CaHa}/^1D_{CaCO}$ global fit ^e	206	73.4	141.0	66.1	6.4	0.47	0.27
steric model ^f		59.2	145.8	51.1	5.3	0.39	-

^a The Euler angles α , β , and γ correspond to clockwise rotations around the $+z$, $+y'$, and $+z''$ axes, where y' is the new y -axis after having rotated around $+z$, and z'' is the new z -axis after having rotated around $+z$ and $+y'$. ^b The axial component of the steric alignment tensor. For the purposes of comparison, D_a values for $^1D_{CaHa}$ and $^1D_{CaCO}$ are normalized relative to $^1D_{NH}$. ^c The rhombicity of the steric alignment tensor. ^d The Cornilescu quality factor (27). ^e The global fits tabulated here differ from those listed above in that the data points corresponding to the RDC outliers shown in Figure 1 are excluded. ^f The predicted steric alignment tensor for the ecT β R2 domain as calculated using the algorithm described by Zweckstetter and Bax (38). The calculation was performed assuming 4% w/v bicelles.

loop segments because of close contacts in the crystalline lattice.

The major points articulated above are supported through the identification RDC outliers, which in the present analysis are defined as RDCs for which the agreement between the experimentally measured and the calculated values differ by more than $2.5\times$ the mean pairwise RMSD among independent experimental measurements. This procedure identifies nine outliers in the case of the comparison to the free structure (Figure 1, left-most panels) and 13 outliers in the case of the comparison to the TGF β -bound structure (Figure 1, right-most panels). The first trend evident upon examination of the 22 data outliers is that among the residues known to contact TGF β directly, only one of them, S52, exhibits an RDC outlier, $^1D_{CaCO}$, when compared to the corresponding RDC value calculated from the TGF β -bound crystal structure but not when compared to the RDC value calculated from the free crystal structure. The elimination of this one outlier lowers the Q factor for the comparison of experimental RDCs to the TGF β -bound crystal structure by an insignificant amount, less than 0.01, thus supporting the first of the two major conclusions stated above.

The experimental observations noted above also agree with predictions based upon comparisons of the free and bound crystal structures. Thus, comparison of the crystal structures, together with the experimentally fitted order tensors, predict significant changes (i.e., a factor of 2 or larger times the experimental error) in just three of the 25 RDC values measured for the 12 amino acid residues that lie within the TGF β binding region. The RDCs identified in this manner include $^1D_{CaCO}$ for S52, $^1D_{NH}$ for I50, and $^1D_{CaHa}$ for E55. The fact that the latter two RDCs do not exhibit the same experimental pattern as that of S52 $^1D_{CaCO}$ is attributed to the differences in the criteria used to identify the predicted

and experimental RDC outliers and is supported by the RDC data in which it is apparent that the experimental and calculated RDCs for these couplings exhibit better agreement to the RDC values calculated from the free crystal structure (Figure 1, open symbols). The overall conclusion drawn from this analysis is that the set of amino acids that comprise the TGF β binding site exhibit experimental RDCs that are in better agreement with the RDC values calculated from the free crystal structure. The underlying reason is related to the small but significant changes in the interfacial contact region indicated by an overlay of the free and bound crystal structures.

The RDC outliers that fall in the noninterfacial region are also shown to exhibit experimental values in better agreement with the RDC values calculated from the free crystal structure. This is evidenced by the larger number of noninterfacial RDC outliers observed in the case of the comparison to the TGF β -bound structure (Figure 1) and by the fact that the Q factors for the fits of the experimental data to the two crystal structures are found to be nearly equal when noninterfacial RDC data outliers are excluded (Table 1). The situation for noninterfacial RDC outliers is, however, to be contrasted to relative to the situation with interfacial RDC outliers as the underlying cause appears to be related to factors other than TGF β binding. Thus, as shown in Figure 1, many of the RDC outliers in the noninterfacial region are found to cluster within the amino acid sequence. The free form of the protein exhibits clusters of RDC outliers between residues 39–40 and 104–105, whereas the TGF β -bound form of the protein exhibits clusters of RDC outliers between residues 39–40, 69–70, and 104–105. The fact that all of the RDC outliers described above map to loop regions, and all exhibit either close contacts in the crystal lattice or elevated B factors (Figure 2), indicates that all of the differences in structure in the noninterfacial region involve alterations in local loop geometries. The fact that these kinds of effects are more pronounced in the case of the TGF β -bound crystal structure explains the differences in the Q factors for the fits of the experimental RDC data to the free and TGF β -bound crystal structures. These observations, taken together, support the second of the two overall conclusions stated above.

Principal χ_1 Rotamer Configurations. Comparison of the free and TGF β -bound crystal structures identifies just nine amino acid residues that exhibit different principal χ_1 rotamers. There is among this subset of nine amino acids residues, two (S52 and E55) that fall within the TGF β binding region of the receptor. Therefore, it was of interest to determine whether the principal χ_1 rotamers for ecT β R2 domain in solution were consistent with those of the free or TGF β -bound crystal structures.

This was accomplished by measuring and quantifying $^3J_{N-H\beta}$ and $^3J_{H\alpha H\beta}$ couplings for the subset of amino acid residues within ecT β R2 that exhibit nondegenerate β -methylene protons (65 out of 88 possible). Experimentally, it was found that among the 65 χ_1 rotamers assigned, all were in agreement with the principal χ_1 rotamer apparent in the free ecT β R2 crystal structure. The experimental data set included χ_1 rotamer assignments for four of the nine amino acid residues shown to adopt different χ_1 rotamer values in the free and TGF β -bound crystal structures, including the interfacial residue S52. Included among the set of residues

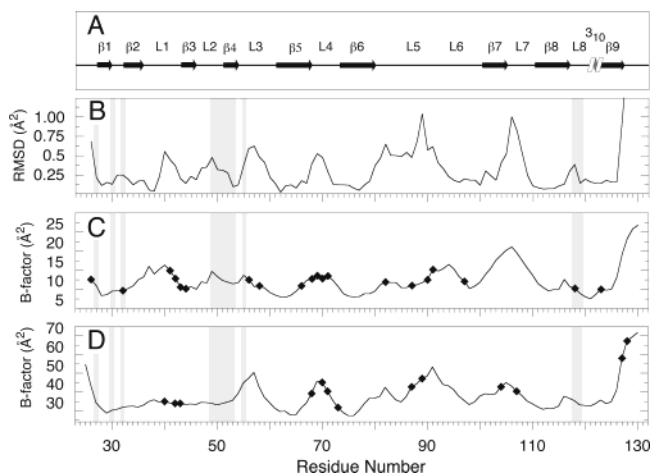


FIGURE 2: *B* factors, crystal contacts, and structural differences between the free and the TGFβ₃-bound forms of ecTβR2. (A) Secondary structure as calculated from the free ecTβR2 crystal structure. (B) Backbone coordinate RMSDs between the crystal structure of the free and the TGFβ₃-bound forms of ecTβR2 plotted as a function of the ecTβR2 amino acid sequence. The structures were aligned by minimizing the deviation between the secondary structural elements. (C and D) Plots of the mean backbone (N, Cα, C) *B* factors as a function of the ecTβR2 amino acid sequence as reported for free (C) (20) and TGFβ₃-bound ecTβR2 (D) (19), respectively. Amino acid residues that exhibit close contacts in the crystal lattice are indicated by the plotted data points. Close contacts are defined as any contacts between ecTβR2 and other molecules in the crystal lattice having a separation of 3.5 Å or less. The vertical gray bars shown in panels B–D indicate amino acid residues that directly contact TGFβ₃ in the crystal structure of the ecTβR2-TGFβ₃ complex.

that exhibited different χ_1 rotamers in the free and bound crystal structures, but which could not be examined because of overlap of their β -methylene protons, was the interfacial residue E55. The fact that the S52 exhibits the same χ_1 rotamer configuration for the free solution and crystal structures, but adopts an altered configuration in the TGFβ₃-bound crystal structure, provides a direct indication that this residue likely reorients from $\chi_1 = -60^\circ$ to $\chi_1 = +180^\circ$ upon binding TGFβ₃. This structural change is in accord with the structural change identified in S52 through the RDC analysis, and as discussed below, may play a role in adaptive binding.

ecTβR2 Solution Structure. The full ecTβR2 3-D solution structure was calculated using the distance geometry-simulated annealing protocol with torsion angle dynamics as implemented in XPLOR-NIH (40, 41). The input data for the calculation consisted of 1519 interresidue NOE distance, dihedral angle, scalar coupling, and RDC restraints. A summary of these restraints, together with the structural statistics, are presented in Table 2. The final ensemble of low-energy structures showed good covalent geometry and low overall energies, with 93% of all residues in the most favored or additionally allowed regions of the Ramachandran plot. There were on average one to two residues per structure that exhibited backbone dihedral angles disallowed in the Ramachandran plot. These invariably mapped to the termini or loop regions where the NMR restraint density was low and thus were not considered significant.

The well-structured portion of the protein, which exhibits a backbone RMSD of 0.79 Å relative to the mean structure, is comprised of residues 26–126 (Table 2). The N- and

Table 2: Structural Statistics for ecTβR2 Free in Solution^a

restraints		
total restraints		1583
NOE distance restraints		
sequential ($ i - j = 1$)		450
short range ($2 \leq i - j \leq 5$)		220
long range ($ i - j > 5$)		498
dihedral restraints		
ϕ		38
ψ		35
χ_1		65
RDC restraints		
¹ D _{NH}		68
¹ D _{CH}		79
¹ D _{CaC'}		72
coupling restraints		
³ J _{HNHα}		58
deviation among ensemble		
bonds (Å)		0.002 ± 0.0002
angles (deg)		0.66 ± 0.02
impropers (deg)		0.59 ± 0.03
dihedral restraints (deg)		2.9 ± 0.5
RDC (Hz)		
¹ D _{NH}		0.9 ± 0.2
¹ D _{CH}		3.7 ± 0.8
¹ D _{CaCO}		0.8 ± 0.1
³ J _{HNHα} restraints (Hz)		0.45 ± 0.03
Ramachandran plot ^b		
most favored (%)		73.7
additionally allowed (%)		19.4
generously allowed (%)		4.3
disallowed (%)		2.7
overall precision		
secondary structure ^c	backbone ^d	0.55
ordered residues ^c	heavy ^d	1.09
	backbone ^d	0.79
	heavy ^d	1.40

^a Structural statistics are calculated for the ensemble of the 10 lowest energy structures. ^b Calculated using the program PROCHECK (65). ^c Secondary structure corresponds to residues 27–29 (β1), 32–35 (β2), 43–44 (β3), 51–53 (β4), 60–68 (β5), 71–79 (β6), 103–105 (β7), 108–115 (β8), 120–122 (3₁₀), and 124–125 (β9). Ordered corresponds to residues 26–126. ^d Backbone atoms include N^H, Cα, and C^O; heavy includes all non-hydrogen atoms.

C-terminal segments, residues 15–25 and 127–136, respectively, exhibit no detectable long-range NOE interactions and are structurally disordered (Figure 4B). These domain boundaries agree to within one residue of the boundaries defined crystallographically (19, 20) and with the results of a TβR2 deletion analysis study (56).

The assigned secondary structure and overall fold of the ecTβR2 NMR structure is highly similar to that reported previously (Figure 3C; Table 2, footnote c) (19, 20). It consists of a large central antiparallel β-sheet, formed by β-strands 2, 6, 5, 8, and 7, packed against a second layer of antiparallel β-sheet formed by β-strands 1, 4, 3, and 9. The regions of assigned secondary structure represent the most well-determined portions of the structure, superimposing relative to the mean with an RMSD of 0.55 Å (Table 2). The primary exception to this is β-strand 7, which includes residues 102–105 in the ensemble of low-energy NMR structures, but which spans residues 99–103 in the crystal structures. This difference appears to be a consequence of the fact that the region between residue 99 and 101 was not assigned and is thus poorly defined.

Comparison of the NMR and Crystal Structures. An overlay of the ensemble of NMR structures with the 1.1 Å

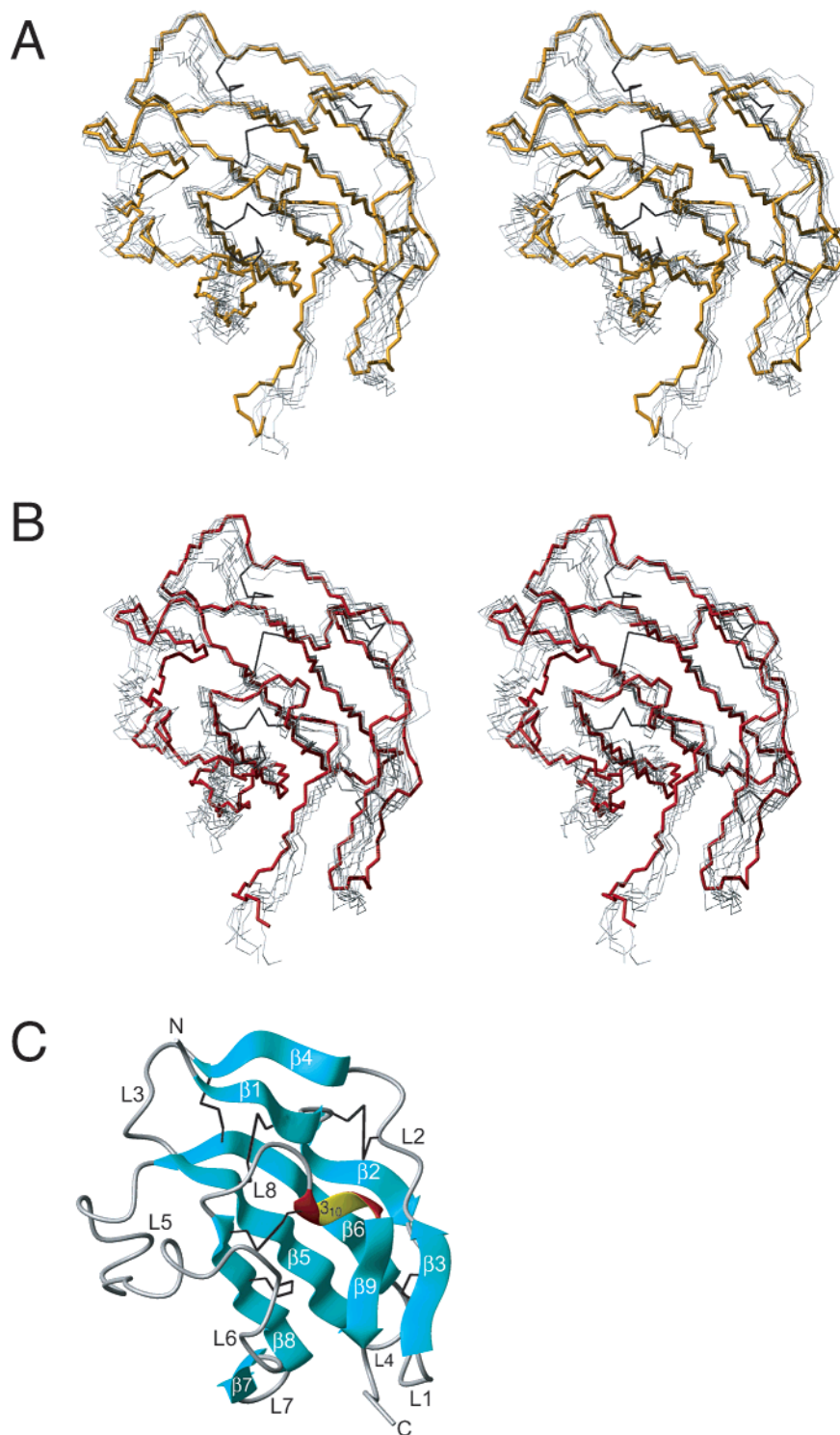


FIGURE 3: $ecT\beta R2$ solution structure and comparison with the crystal structures of free and $TGF\beta 3$ -bound $ecT\beta R2$. (A) The 10 lowest energy $ecT\beta R2$ solution structures (gray) superimposed with the crystal structure (dark yellow) of free $TGF\beta 3$ (20). The structures are aligned based upon the deduced secondary structure of the $ecT\beta R2$ NMR structure (Table 2, footnote c). (B) The 10 lowest energy $ecT\beta R2$ solution structures (gray) superimposed with the crystal structure (red) of $ecT\beta R2$ -bound $TGF\beta 3$ (19). The structures are aligned as in panel A. (C) Ribbon diagram of the regularized average $ecT\beta R2$ solution structure. The elements of regular secondary structure ($\beta 1$ – $\beta 9$, 3_{10}) were determined using the criterion established by Kabsch and Sander (67). Loop regions are designated L1 to L8. This figure was prepared using the program MOLMOL (68).

free and 2.2 Å $TGF\beta 3$ -bound $ecT\beta R2$ crystal structures is shown in Figure 3 (panels A and B, respectively). The structures are remarkably similar, superimposing with backbone RMSDs of 0.96 and 0.95 Å over the regions of assigned secondary structure and 1.38 and 1.36 Å over the structurally ordered regions, respectively (Table 3). The overall similarity

of the solution and crystal structures shows that any systematic structural perturbations caused by $TGF\beta$ binding, lattice packing, or other effects must fall below an overall value of 1.0 Å or less.

The data shown in panel B of Figure 4 reveal that the residues that comprise the $TGF\beta$ binding region are well-

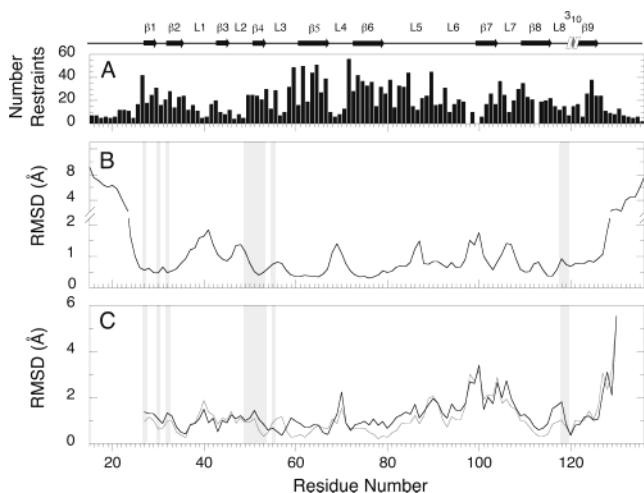


FIGURE 4: Precision of the calculated ensemble and structural differences relative to the crystal structures of free and TGFβ3-bound ecTβR2. (A) The number of interresidue NOE distance restraints on a per residue basis. (B) Plot of residue RMSDs for the ensemble of accepted structures relative to the mean structure. (C) Backbone RMSDs for the regularized average ecTβR2 structure versus the crystal structures of free (solid black line) and TGFβ3-bound ecTβR2 (solid gray line). The vertical gray bars shown in panels B and C indicate amino acid residues that directly contact TGFβ in the crystal structure of the ecTβR2-TGFβ3 complex.

Table 3: Coordinate RMS Deviations for NMR Ensemble versus Crystal Structures of Free and TGFβ3-Bound ecTβR2^a

		free	TGFβ3-bound
secondary structure ^c	backbone ^b	0.96	0.95
	heavy ^b	1.67	1.66
ordered residues ^c	backbone ^b	1.38	1.36
	heavy ^b	2.16	2.24

^a Structural statistics are calculated for the ensemble of 10 lowest energy structures; RMSD values are in units of angstroms. ^b Backbone atoms include N^H, Cα, and C^O; heavy includes all non-hydrogen atoms. ^c Secondary structure corresponds to residues 27–29 (β1), 32–35 (β2), 43–44 (β3), 51–53 (β4), 60–68 (β5), 71–79 (β6), 103–105 (β7), 108–115 (β8), 120–122 (3₁₀), and 124–125 (β9). Ordered corresponds to residues 26–126.

defined by the available NMR data, falling in regions of the structure that are determined to a precision of 0.5–0.8 Å. The three loop regions, 1, 4, and 7, identified by analysis of the RDC data as exhibiting structural differences relative to the crystal structures, are more poorly defined by the available NMR data, exhibiting values of precision that vary from about 1.4–1.8 Å. The plots of the backbone coordinate deviation between the NMR structure and the free and TGFβ3-bound crystal structures are shown in panel C of Figure 4 (solid black and gray lines, respectively). The absolute deviations between the NMR structures and the crystal structures are found to be 0.7–1.3 Å for residues within the binding region and 1.5–2.0 Å for loops 1, 4, and 7.

The data presented above indicate that the structural results are not sufficient to permit an unambiguous determination as to whether the differences identified through analysis of the RDC and χ_1 data are real. This follows, as the structural differences in the binding region and in the loops are comparable to the corresponding coordinate precision, indicating that any differences detected are unlikely to be statistically significant. The overall conclusion drawn from the combined structural analysis is that the solution

structure of ecTβR2 is found to be very similar to that of the free and TGFβ3-bound crystal structures, superimposing with an overall backbone RMSD of about 1.0 Å. The minor structural perturbations in the loops and binding region indicated by the RDC data likely exist, although these changes are difficult to detect through comparison of the full 3-D structures.

Internal Flexibility of the ecTβR2 Domain. The internal flexibility of the ecTβR2 domain has been investigated by measuring in duplicate at a ¹⁵N frequency of 60.8 MHz backbone ¹⁵N T₁, ¹⁵N T₂, and ¹⁵N–{¹H} NOE relaxation parameters. The average pairwise RMSD values of the two T₁, T₂, and NOE measurements was 1.4, 1.7, and 4.1%, respectively. These average pairwise errors are approximately equal to the average Monte Carlo error for each data set multiplied by $\sqrt{2}$, indicating that the errors in the measured data arise predominantly from random noise.

The experimental relaxation data were modeled assuming axial diffusional anisotropy (45). The inclusion of the axially symmetric diffusion tensor in the model-free calculations was justified by the correspondence of the experimental tensor with the tensor estimated from inertia calculations. The axially symmetric tensor was further supported by the overall χ^2 value for the fit, 5.64, which is significantly lower than that obtained for an isotropic model, 10.85, or for an axially symmetric model with randomized N–H bond vector orientations, 9.53. Attempts were also made to model the experimental relaxation data using a fully asymmetric diffusion tensor (46). These fits, however, were not considered statistically significant, as the experimentally determined tensor was not defined by a distinct minimum, and the overall χ^2 value for the fit, 4.80, was not significantly lower as compared to that obtained for the axially symmetric tensor, 5.64. These data are summarized in Table 4.

Model-free analyses were performed using the program ModelFree4 (52) with N–H bond vector orientations derived from the lowest energy NMR structure and the parameters describing the axially symmetric diffusion tensor listed in Table 4. Model selection was performed using the *F* test strategy described by Mandel et al. (52). This procedure yielded statistically significant fits for all residues, except F24 and R66. Profiles of S^2 , τ_e , R_{ex} , and S_f^2 derived in this manner are plotted in Figure 5. As expected, residues in the N- and C-terminal regions, residues 15–25 and 126–136, respectively, have low S^2 or S_f^2 values. The remaining residues have S^2 values greater than 0.75, indicating that the backbone is relatively rigid on the ns to ps time scale over the length of the structured core. There are, however, a few exceptions to this generalization. Moderately decreased S^2 or S_f^2 values and higher τ_e values are evident for residues located near the tips of loops L1, L4, L5, and L7 (Figure 5).

There are also a relatively large number of residues that undergo motions on the ms to μ s time scales, as satisfactory model-free fits of the relaxation data required nonzero R_{ex} terms for 23 residues. As shown in Figure 5, these are clustered around residues 26–28, 39–60, 69–70, and 110–119. An interesting feature of these data is that the residues exhibiting the largest R_{ex} values are either cysteine residues themselves (C28, C54) or residues directly adjacent to cysteine residues (A60, which precedes C61). The fact that C28 is connected to C61 via a disulfide bond suggests that

Table 4: Modeling of the ecT β R2 Diffusion Tensor

A. Experimental Data Fitted to Isotropic and Axially Symmetric Diffusion Tensors						
model	NH vectors	θ (deg)	φ (deg)	D_{\parallel}/D_{\perp}	τ_{av} (ns) ^a	χ^2 ^b
isotropic					8.10	10.85
axially symmetric	crystal ^c	141.8	105.5	1.27	8.09	6.73
axially symmetric	NMR ^d	145.7 \pm 2.8	99.5 \pm 8.2	1.32 \pm 0.04	8.11 \pm 0.02	5.64 \pm 0.43
axially symmetric	random ^e	101.3 \pm 32.3	100.4 \pm 56.3	0.97 \pm 0.10	8.02 \pm 0.04	9.53 \pm 0.72
B. Hydrodynamic Modeling of the Axially Symmetric Diffusion Tensor ^f						
structure	residue range	θ (deg)	φ (deg)	D_{\parallel}/D_{\perp}		
crystal	25–130	146.0	113.7	1.28		
NMR ^c	25–130	147.1 \pm 2.4	104.3 \pm 5.2	1.28 \pm 0.03		
NMR ^c	15–136	153.4 \pm 6.7	100.4 \pm 9.7	1.51 \pm 0.12		

^a The average correlation time defined according to the convention described by Woessner (66). ^b Normalized value of χ^2 defined according to eq 4. ^c NH bond vector orientations were calculated from the crystal structure of free ecT β R2. ^d Values reported for the NMR structure correspond to the mean and standard deviation of the values obtained from using NH bond vector orientations from the 10 lowest energy NMR structures. ^e Random indicates average values and standard deviations obtained from fitting 110 different test data sets using NH bond vector tables in which the residue numbers had been randomized (see Experimental Procedures). ^f Parameters described here were based upon the calculated inertia tensor: $\mathbf{I}_{xx}/\mathbf{I}_{yy}/\mathbf{I}_{zz}$ 1.00:1.05:0.71. On this basis, the tensor was approximated as having axial symmetry with the principal axis lying along \mathbf{I}_{zz} . The axial ratio, D_{\parallel}/D_{\perp} , was calculated from eq 1.

some type of motion involving the disulfide itself might underlie the broadening evident for these two amino acid residues. Similarly, C54 exhibits an elevated R_{ex} value, while the backbone amide of the residue to which it is linked, C78, was not assigned and as indicated is also likely broadened by exchange.

There are, in addition to the residues mentioned above, several additional residues that required smaller R_{ex} terms to be adequately fit using the Lipari–Szabo model. These fall into three clusters, one between residues 39–58, another between residues 69–70, and the third between residues 110–119. Distributed among the first and third clusters are five amino acids, residues 49, 52, 55, 118, and 119, which comprise roughly one-half of the amino acids that contact TGF β 3 in the crystal structure of the ecT β R2–TGF β 3 complex (Figure 5C, open symbols). The remaining sites in the first and third clusters, residues 39, 40, 43–47, 56, 58, 110, 111, and 116, are not presently known to be functionally relevant. It is nevertheless interesting to note that these, along with other residues whose backbone amide resonances were not assigned, form a contiguous patch on the surface of the molecule in a position both adjacent to the binding site for TGF β and adjacent to the proposed surface through which the T β R2 extracellular domain interacts with the T β R1 extracellular domain (Figure 7) (19). The second cluster (residues 69–70) falls at the apex of a solvent exposed β hairpin. These two residues are well-conserved among T β R2s from different species (19), although the functional significance, or the lack thereof for these two residues, is not known.

DISCUSSION

T β R2 Binds TGF β with High Affinity. T β R2 plays a pivotal role in the TGF β signaling pathway by functioning as the sensor responsible for detecting the presence of TGF β in the extracellular space and for triggering the signaling cascade that ultimately sends a TGF β -specific signal to the cell nucleus (2). Compatible with its biological role, T β R2 binds TGF β with high affinity. Estimates for the magnitude of the disassociation constant between ecT β R2 and TGF β 1

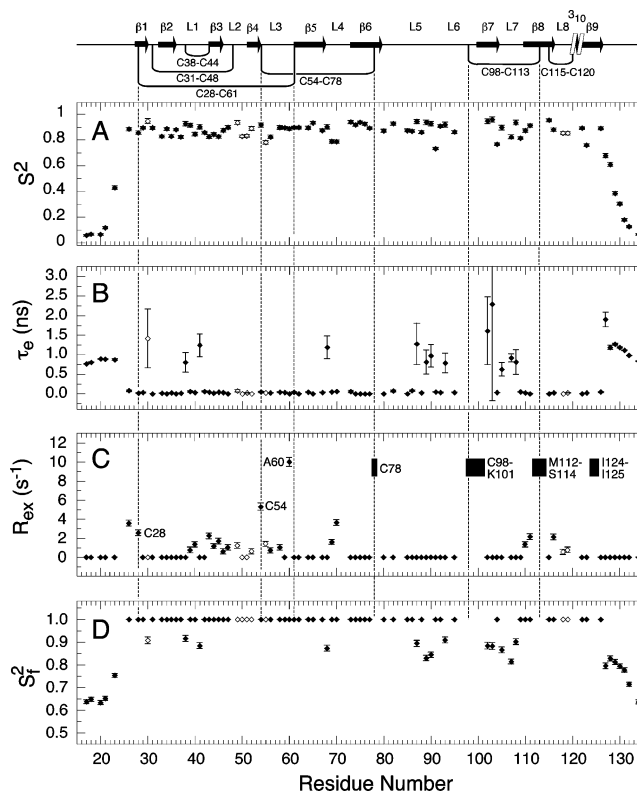


FIGURE 5: Model-free parameters S^2 , τ_e , R_{ex} , and S_f^2 of backbone amides derived from analysis of the ecT β R2 ^{15}N T_1 , ^{15}N T_2 , and ^{15}N – $\{^1\text{H}\}$ NOE data recorded at 27 $^\circ\text{C}$. The modeling was carried out assuming an axially symmetric diffusion tensor with $D_{\parallel}/D_{\perp} = 1.32$, $\tau_{\text{avg}} = 8.11$ ns, and N–H bond vector information derived from the lowest energy model of the ecT β R2 solution structure. Data points having a value of exactly 0.0 in panels B and C, or 1.0 in panel D, indicate that this parameter was not included in the motional model. Solid black bars shown in the upper portion of panel C indicate amino acid residues whose backbone amide protons were not detected during the course of the sequential assignment process. The secondary structure and disulfide bonding pattern for the T β R2 extracellular domain is indicated in the upper portion of the figure. A complete listing of the experimental relaxation data and model-free parameters is provided as Supporting Information.

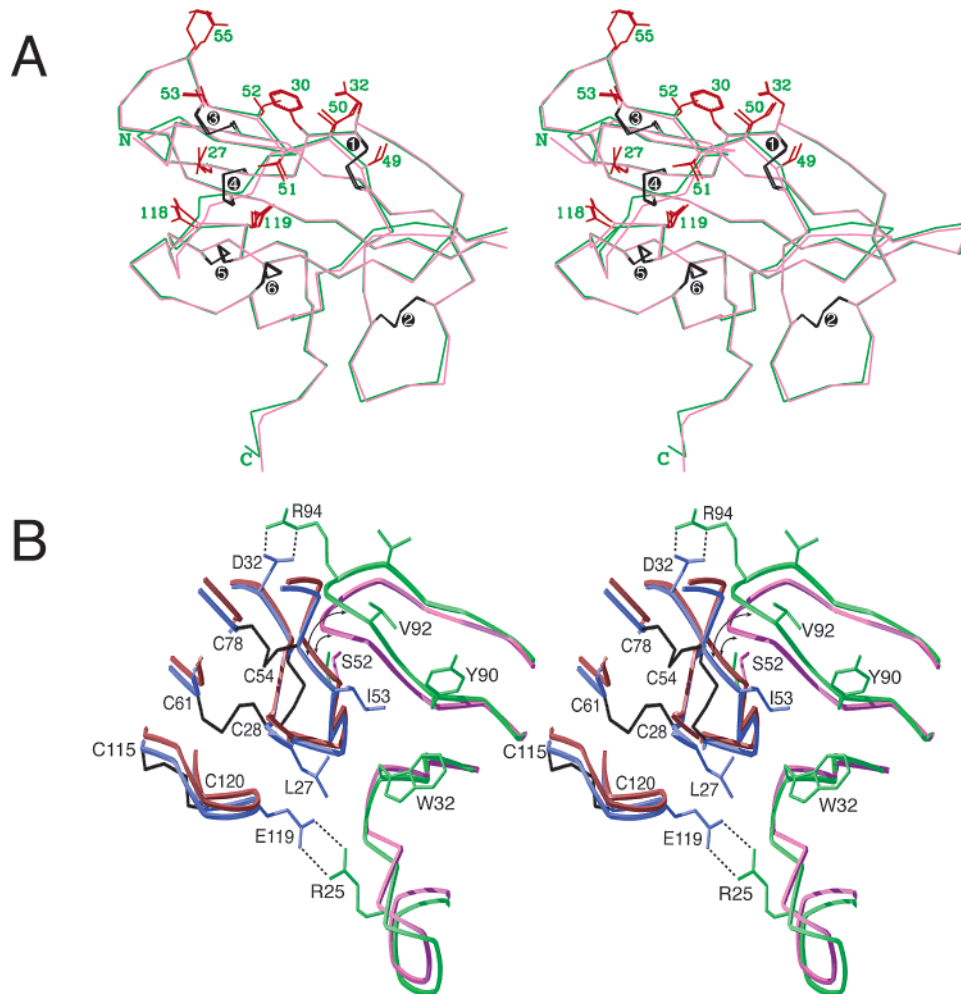


FIGURE 6: Binding induced structural perturbations in ecT β R2 and TGF β 3 as depicted through structural alignments of the free and bound crystal structures. (A) Structural alignment of the crystal structures of the free (20) and TGF β 3-bound (19) forms of ecT β R2. Structures are depicted as C α traces (bound—pink; free—green) and are aligned by a least-squares fit of the assigned secondary structure. Side chains of the 11 TGF β contact residues are shown in red and are labeled by their residue numbers. Disulfide bonds are shown in black and are labeled as follows: (1) C31—C48, (2) C38—C44, (3) C54—C78, (4) C28—C61, (5) C98—C113, and (6) C115—C120. (B) A depiction of the ecT β R2-TGF β 3 contact region and possible binding induced structural perturbations in both ecT β R2 and TGF β 3. The figure was constructed by superimposing the crystal structures of free ecT β R2 and free TGF β 3 with the corresponding components in the crystal structure of the ecT β R2-TGF β 3 complex. The superimpositions were done in each case by minimizing the coordinate difference between the elements of regular secondary structure. The free and bound ecT β R2 structures are shown in red and blue, respectively. The free and bound TGF β 3 structures are shown in magenta and green, respectively. The curved arrows, at the point of closest contact between the ecT β R2 and the TGF β 3 structures, depict the increase in separation between the two that presumably occurs upon binding.

vary from about $5 \times 10^{-9} \text{ M}^{-1}$ as assessed by a purified component binding assay (57) to about $5 \times 10^{-8} \text{ M}^{-1}$ as assessed by measuring the antagonist activity of ecT β R2 in a cell-based proliferation assay (57).

Recently, the 2.2 Å crystal structure of the ecT β R2-TGF β 3 complex was reported (19). This structure established the overall architecture of the ecT β R2-TGF β complex and revealed that ecT β R2 binds TGF β by inserting β -strand 4, T51-S52-I53, together with flanking residues S49-I50 and E55, into a cleft between the extended finger segments of TGF β . Inspection of the binding interface reveals that the residues of ecT β R2 that likely contribute the most to the affinity include I53 and L27, which lie within a hydrophobic pocket formed by TGF β 3 residues W32, Y91, and V92, together with D32 and E119, which form ion pairs with TGF β 3 R94 and R25, respectively (19). These features of the ecT β R2-TGF β 3 binding interface are depicted in Figure 6B.

The studies reported here, together with comparisons of the ecT β R2 solution structure to the TGF β 3-bound ecT β R2 crystal structure, provide several new inferences with respect to the kinds of changes in structure and flexibility in the T β R2 extracellular domain that likely occur upon TGF β binding. These include the fact that the structural perturbations that occur upon binding are minor and that flexibility within the receptor on the ms to μ s time scale likely plays an important role in adaptive binding.

T β R2 and TGF β Bind with Only a Minor Component of Induced Fit Character. The solution structure of ecT β R2 was compared to the 1.1 Å free and 2.2 Å TGF β 3-bound ecT β R2 crystal structures through comparison of H^N—N^H, H ^{α} —C ^{α} , and C ^{α} —C^O bond vector orientations, through the determination of χ_1 rotamer conformations, and through a full 3-D structural analysis. The results revealed that the solution structure of the T β R2 domain is highly similar to both the free and the TGF β 3-bound crystal structures. The extent of

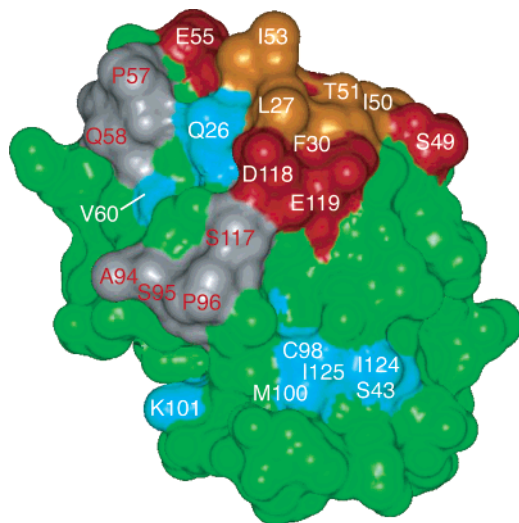


FIGURE 7: Relative disposition of the TGF β binding site to other regions exhibiting slow (ms to μ s) time scale motion in the T β R2 extracellular domain. This is depicted through a surface representation of the ecT β R2 domain in which interfacial and noninterfacial residues that required an R_{ex} correction in the Lipari–Szabo modeling are shown in red and blue, respectively. Other interfacial amino acid residues that did not require a R_{ex} correction in the Lipari–Szabo modeling are depicted in orange. Putative contact sites with the T β R1 extracellular domain identified by Hart et al. (19) are depicted in gray.

this similarity, as assessed by backbone superimpositions of the ensemble of low-energy NMR structures with the free and TGF β 3-bound crystal structures, was found to be about 1.4 Å for each over the structurally ordered regions and about 0.95 Å for each over the regions of secondary structure. The limited precision of the NMR structures, 0.79 Å overall and 0.55 Å over the regions of secondary structure, together with the subtle structural differences evident between the free and the TGF β 3-bound crystal structures, precluded efforts to directly identify any systematic differences in structure between the free and bound states.

Despite this, there does appear to be a subtle structural difference in the TGF β binding region, as indicated by a comparison of both the RDC data and the χ_1 data, to the corresponding parameters predicted by the TGF β 3-bound crystal structure. This structural change involves a change in the backbone conformation of S52, coupled with a change in its principal χ_1 rotamer conformation from -60° in the free state to $+180^\circ$ in the bound state. The evidence indicating this structural change is caused by TGF β binding follows from the similarity of experimental RDC and χ_1 data for S52 with the corresponding values predicted from the free crystal structure, but not the TGF β 3-bound structure, and by the fact that the binding region of the TGF β 3-bound crystal structure is not altered by other factors, such as close contacts in the crystalline lattice, or elevated B factors (Figure 2D).

The structural change indicated by the RDC and χ_1 data is illustrated in Figure 6A, where the free and TGF β 3-bound crystal structures have been overlaid, and the side chains of residues that contact TGF β have been displayed. The structural features that indicate a perturbation in the binding region include altered χ_1 rotamers for S52, along with a systematic shift of the backbone of the exposed ridge away from the side of the binding surface containing D32, toward

the opposite side of the binding surface containing E119. The average shift in backbone atom coordinates is 0.35 Å over the segment from residue S49 to E55 and 0.29 Å over residues T51–I53 (β -strand 4). These shifts are not particularly large, although they are notably larger than that observed for any other segment of three amino acids found within all other regular elements of secondary structure and nearly twice the average deviation over all elements of regular secondary structure (0.16 Å).

The previously reported comparison of the free and bound forms of TGF β 3 revealed similar conformational changes (19). The largest of these involved a shift of the finger segment containing R94 away from the tip of the opposite finger segment containing R25. This structural change, which involves a displacement by about 1.5 Å at the tip of the finger containing R94, is likely facilitated by the flexibility inherent in this region of the structure, as recently shown through NMR studies of the uncomplexed form of TGF β 3 (24). The side chains of the T β R2 contact residues R25, W32, and R94 are also observed to reorient upon TGF β 3 binding.

These changes in structure are depicted by an overlay of the free and bound TGF β 3 and ecT β R2 crystal structures shown in Figure 6B. The adjustments in backbone conformation described above lead to an increase in the separation between the point of closest contact between the backbones of TGF β 3 and ecT β R2, ecT β R2 S52 and TGF β 3 V92, from about 1.3 Å in the uncomplexed state to about 3.1 Å in the complexed state (Figure 6B, curved arrows). S52, as discussed, is shown to reorient, such that the side chain hydroxyl rotates away from the point of closest contact with TGF β , toward the receptor. These changes eliminate steric contacts that would otherwise occur between ecT β R2 S52 and the backbone of the TGF β fingertip segment containing R94, and are thus likely important for enabling ecT β R2 to bind more deeply in the cleft between the TGF β fingertips. Hence, while ecT β R2 and TGF β engage one another through surfaces that are largely preformed, there is a minor component of induced fit character within both components, which appears to be important for enabling the two to interact with high affinity.

Potential Relationships of Flexibility to Binding. Changes in conformational entropy are also expected to strongly influence the overall binding affinity. Recent examples have shown that restriction of internal backbone or side chain flexibility in the uncomplexed state (58, 59) or enhanced backbone or side chain flexibility in the complexed state (59) are possible mechanisms by which binding-induced decreases in conformational entropy can be minimized or eliminated altogether.

The constrained nature of the T β R2 TGF β binding surface indicates that conformational restriction of the free receptor may contribute to its high affinity for the TGF β isoforms. Included within this surface are β -strands 1 and 4, which are arranged in an antiparallel fashion and are tethered to the underlying structured core by two disulfide-bonded cysteine residues (C28, which is bonded to C61, and C54, which is bonded to C78; Figure 5). The binding surface also includes residues D118 and E119, which are located at the tip of loop 8 and are also constrained by a disulfide, C115–C120.

The experimental NMR relaxation data presented here support the conformational restriction model. The plot of S^2

values as a function of residue number reveals that none of the residues within the TGF β binding region of uncomplexed eT β R2 have values lower than 0.78 (Figure 5C, open symbols). The data further reveal averaged Lipari–Szabo S^2 values of 0.86 over the residues that comprise the TGF β binding surface and 0.88 over the residues that comprise the secondary structure. The fact that the averaged S^2 value for the TGF β binding region is comparable to that of the secondary structure, and is as high or higher than that found in the well-ordered regions of other proteins, indicates that the backbone of the TGF β binding site is restricted in terms of its internal flexibility on the ns to ps time scale. This, together with the fact that the S^2 values are unlikely to become significantly higher than 0.86 upon binding, supports the entropic restriction model stated above, at least in a qualitative sense, and at least for backbone motions occurring on the ns to ps time scale.

The fact that the T β R2 extracellular domain binds TGF β with a minor component of induced fit character is of interest as the relaxation data further reveal that the T β R2 extracellular domain exhibits ms to μ s time scale motions in TGF β binding residues C28, S49, S52, C54, E55, D118, and E119. Altogether, nearly two-thirds of the total residues within TGF β binding surface undergo motion on the ms to μ s time scale. The observation of the slow time scale motions in the TGF β binding region has two possible mechanistic interpretations.

The first is that the uncomplexed protein exists as an equilibrium mixture of conformations, the form that predominates in the uncomplexed state and the form that predominates in the complexed state. This kind of conformational transition has been noted in several other interacting systems (60) and is significant from the standpoint that such a transition may enable the receptor to adopt a conformation that maximizes favorable contacts in the complex. The type of process that could give rise to the observed slow time scale motion in the T β R2 extracellular domain involves the rearrangement of the exposed TGF β binding ridge between the conformation that predominates in the uncomplexed form of the protein and the conformation that predominates in the complexed form of the protein. The second possibility differs relative to the first in that it is no longer assumed that the underlying conformational transition is of direct functional relevance. The underlying flexibility may nevertheless indirectly contribute to the affinity, by enabling minor adjustments in conformation important for maximizing favorable contacts in the interface.

The latter phenomenon has been indicated in numerous other interacting proteins, although it has been best characterized in basic pancreatic trypsin inhibitor (BPTI) (61, 62). These studies have shown that the C14–C38 disulfide bond, which tethers the protease binding loop to the underlying structured core, adopts two distinct conformations that differ with respect to the isomeric state of the C14–C38 disulfide bond (63). It has been further shown that selective reduction of the C14–C38 disulfide bond fails to eliminate the source of the slow time scale motion in the protease binding loop, reinforcing the notion that it is the limited packing density in the binding region responsible for the slow time scale motions in the protease binding loop, not the disulfide itself (64).

There is some indication that this type of phenomenon may also occur in the context of the T β R2 extracellular domain. The qualitative estimates of the exchange rates obtained from the Lipari–Szabo modeling reveal significant slow time scale motions in the cysteine residues, C28 and C54, which tether the TGF β binding ridge to the underlying structured core. The data as noted further reveal the presence of slow time scale motion adjacent to or within the cysteine residues to which C28 and C54 are bonded (C61 and C78, respectively). Thus, in analogy to BPTI, it is conceivable that the slow time scale motion in the binding region of eT β R2 reflects the fact that the C28–C61 and C54–C78 disulfide bonds are not restricted to a single isomeric state.

The fact that the T β R2 extracellular domain and BPTI exhibit such remarkably similar physical properties makes it tempting to speculate that each have evolved similar mechanisms to bind their target proteins with high affinity and specificity. The critical features of such a mechanism would include the use of an exposed, but conformationally restricted, loop or ridge, with a minor component of residual internal flexibility, so as to enable adaptive binding as necessary. This temptation is best resisted, however, owing to the qualitative nature of the R_{ex} values determined in the present study and the possibility that the slow time scale motion evident in the binding region may be due to another type of ms to μ s conformational process, such as flipping of one of the nearby aromatic rings, such as that of F30 or Y85.

The T β R2 extracellular domain, in addition to functioning as the sensor responsible for detecting the presence of TGF β in the extracellular space, has also been shown to trigger the intracellular component of the TGF β pathway by facilitating the recruitment of T β R1 into the T β R2–TGF β complex. The mechanism by which this occurs is not known, although modeling studies indicate that this might be mediated by contacts between the T β R2 and the T β R1 extracellular domains (19). The putative surface through which the T β R1 extracellular domain contacts the T β R2 extracellular domain is shown in Figure 7 (gray shading). This interaction surface is shown to map to a position adjacent to, but not overlapping, the additional sites of ms to μ s time scale motion experimentally identified in the T β R2 extracellular domain (blue shading). Thus, as an alternative to the original proposal, the region of additional slow time scale motion may correspond to the true binding surface; the lack of coincidence between the newly proposed and the surface proposed based on modeling may simply be a consequence of inaccuracies in the modeling.

Conclusions. The NMR data presented here have shown that the structure of the T β R2 extracellular domain in solution exhibits only very minor differences relative to the crystal structure of the TGF β -bound form. The NMR data have further shown that the T β R2 extracellular domain exhibits little internal flexibility on the ns to ps time scale over the length of the structured core. The lack of significant structural changes, together with the limited flexibility on fast time scales, indicates that conformational restriction of the uncomplexed T β R2 extracellular domain likely contributes to its affinity for binding the TGF β isoforms. There, is however, limited ms to μ s time scale motion occurring in the TGF β binding region. The source of the slow time scale motion in the TGF β binding surface is not known with certainty. Regardless of the source, and regardless of whether the

motion enables a direct conformational transition between uncomplexed and complexed states, this motion may enable the T β R2 extracellular to undergo minor adjustments in conformation necessary to maximize favorable contacts in the complex with TGF β .

ACKNOWLEDGMENT

We gratefully acknowledge Ad Bax for the IPAP-HSQC pulse program and the RDC analysis package PALES, Frank Delaglio for the NMR processing package nmrPipe, Nico Tjandra for C-programs for calculating the diffusion tensor, Marius Clore for XPLOR-NIH, Art Palmer for the Lipari–Szabo modeling program ModelFree4, Alex Taylor for assistance in analysis of the crystal contacts, and Darón Freedberg and Barry Nall for useful comments.

SUPPORTING INFORMATION AVAILABLE

Tables listing ^{15}N T $_1$, ^{15}N T $_2$, and ^{15}N –{ ^1H } NOE data and model-free parameters for ecT β R2 at 27 °C. This material is available free of charge via the Internet at <http://pubs.acs.org>.

REFERENCES

- Roberts, A. B., and Sporn, M. B. (1990) in *Peptide Growth Factors and Their Receptors* (Roberts, A. B., and Sporn, M. B., Eds.) pp 421–472, Springer-Verlag, Heidelberg, Germany.
- Massague, J. (1998) *Annu. Rev. Biochem.* 67, 753–791.
- Luo, K., and Lodish, H. (1996) *EMBO J.* 15, 4485–4496.
- Weis-Garcia, F., and Massagué, J. (1996) *EMBO J.* 15, 276–289.
- Wrana, J. L., Attisano, L., Wiesner, R., Ventura, F., and Massagué, J. (1994) *Nature* 370, 341–347.
- Massague, J., Hata, A., and Liu, F. (1997) *Trends Cell Biol.* 7, 187–192.
- Markowitz, S. D., and Roberts, A. B. (1996) *Cytokine Growth Factor Rev.* 7, 93–102.
- Massague, J., Blain, S. W., and Lo, R. S. (2000) *Cell* 103, 295–309.
- Reiss, M. (1999) *Microbes Infect.* 1, 1327–1347.
- Arteaga, C. L., Hurd, S. D., Winnier, A. R., Johnson, M. D., Fendly, B. M., and Forbes, J. T. (1993) *J. Clin. Invest.* 92, 2569–2576.
- Sun, L., and Chen, C. (1997) *J. Biol. Chem.* 272, 25367–25372.
- Bandyopadhyay, A., Zhu, Y., Cibull, M. L., Bao, L., Chen, C., and Sun, L. (1999) *Cancer Res.* 59, 5041–5046.
- Bandyopadhyay, A., Zhu, Y., Malik, S. N., Kreisberg, J., Brattain, M. G., Sprague, E. A., Luo, J., Lopez-Casillas, F., and Sun, L. Z. (2002) *Oncogene* 21, 3541–3551.
- Yin, J. J., Selander, K., Chirgwin, J. M., Dallas, M., Grubbs, B. G., Wieser, R., Massague, J., Mundy, G. R., and Guise, T. A. (1999) *J. Clin. Invest.* 103, 197–206.
- Kakonen, S. M., Selander, K. S., Chirgwin, J. M., Yin, J. J., Burns, S., Rankin, W. A., Grubbs, B. G., Dallas, M., Cui, Y., and Guise, T. A. (2002) *J. Biol. Chem.* 277, 24571–24578.
- Bottinger, E. P., Jakubczak, J. L., Haines, D. C., Bagnall, K., and Wakefield, L. M. (1997) *Cancer Res.* 57, 5564–5570.
- Fakhrai, H., Dorigo, O., Shawler, D. L., Lin, H., Mercola, D., Black, K. L., Royston, I., and Sobol, R. E. (1996) *Proc. Natl. Acad. Sci. U.S.A.* 93, 2909–2914.
- Cheifetz, S., Hernandez, H., Laiho, M., ten Dijke, P., Iwata, K. K., and Massague, J. (1990) *J. Biol. Chem.* 265, 20533–20538.
- Hart, P. J., Deep, S., Taylor, A. B., Shu, Z., Hinck, C. S., and Hinck, A. P. (2002) *Nature Struct. Biol.* 9, 203–208.
- Boesen, C. C., Radaev, S., Motyka, S. A., Patamawenu, A., and Sun, P. D. (2002) *Structure* 10, 913–919.
- Mittl, P. R. E., Priestle, J. P., Cox, D. A., McMaster, G., Cerletti, N., and Grutter, M. G. (1996) *Protein Sci.* 5, 1261–1271.
- Pellaud, J., Schote, U., Arvinte, T., and Seelig, J. (1999) *J. Biol. Chem.* 274, 7699–7704.
- Bocharov, E. V., Blommers, M. J., Kuhla, J., Arvinte, T., Burgi, R., and Arseniev, A. S. (2000) *J. Biomol. NMR* 16, 179–180.
- Bocharov, E. V., Korzhnev, D. M., Blommers, M. J., Arvinte, T., Orekhov, V. Y., Billeter, M., and Arseniev, A. S. (2002) *J. Biol. Chem.* 277, 43104–43109.
- Kirsch, T., Sebald, W., and Dreyer, M. K. (2000) *Nat. Struct. Biol.* 7, 492–496.
- Hinck, A. P., Walker, K. P., III, Martin, N. R., Deep, S., Hinck, C. S., and Freedberg, D. I. (2000) *J. Biomol. NMR* 18, 369–370.
- Cornilescu, G., Delaglio, F., and Bax, A. (1999) *J. Biomol. NMR* 13, 289–302.
- Grzesiek, S., Kuboniwa, H., Hinck, A. P., and Bax, A. (1995) *J. Am. Chem. Soc.* 117, 5312–5315.
- Archer, S. J., Ikura, M., Torchia, D. A., and Bax, A. (1991) *J. Magn. Reson.* 95, 636–641.
- Vuister, G., and Bax, A. (1993) *J. Am. Chem. Soc.* 115, 7772–7777.
- Suri, A. K., and Levy, R. M. (1993) *J. Magn. Reson., Ser. B* 101, 320–324.
- Suri, A. K., and Levy, R. M. (1995) *J. Magn. Reson., Ser. B* 106, 24–31.
- Ottiger, M., and Bax, A. (1999) *J. Biomol. NMR* 13, 187–191.
- Ottiger, M., Delaglio, F., and Bax, A. (1998) *J. Magn. Reson.* 131, 373–378.
- Grzesiek, S., and Bax, A. (1992) *J. Magn. Reson.* 96, 432–440.
- Tjandra, N., and Bax, A. (1997) *J. Am. Chem. Soc.* 119, 9576–9577.
- Delaglio, F., Grzesiek, S., Vuister, G., Zhu, W., Pfeifer, J., and Bax, A. (1995) *J. Biomol. NMR* 6, 277–293.
- Zweckstetter, M., and Bax, A. (2000) *J. Am. Chem. Soc.* 122, 3791–3792.
- Nilges, M., Clore, G. M., and Gronenborn, A. M. (1988) *FEBS Lett.* 239, 129–136.
- Schwieters, C. D., and Clore, G. M. (2001) *J. Magn. Reson.* 152, 288–302.
- Schwieters, C. D., Kuszewski, J. J., Tjandra, N., and Clore, G. M. (2003) *J. Magn. Reson.* 160, 65–73.
- Kay, L. E., Nicholson, L. K., Delaglio, F., Bax, A., and Torchia, D. A. (1992) *J. Magn. Reson.* 97, 359–375.
- Press, W. H., Flannery, B. P., Teukolsky, S. A., and Vetterling, W. T. (1988) *Numerical Recipes in C*, Cambridge University Press, Cambridge, UK.
- Freedberg, D. I., Ishima, R., Jacob, J., Wang, Y. X., Kustanovich, I., Louis, J. M., and Torchia, D. A. (2002) *Protein Sci.* 11, 221–232.
- Tjandra, N., Feller, S. E., Pastor, R., and Bax, A. (1995) *J. Am. Chem. Soc.* 117, 12562.
- Tjandra, N., Wingfield, P., Stahl, S., and Bax, A. (1996) *J. Biomol. NMR* 8, 273–284.
- Barbato, G., Ikura, M., Kay, L. E., Pastor, R. W., and Bax, A. (1992) *Biochemistry* 31, 5269–5278.
- Copie, V., Tomita, Y., Akiyama, S. K., Aota, S., Yamada, K. M., Venable, R. M., Pastor, R. W., Krueger, S., and Torchia, D. A. (1998) *J. Mol. Biol.* 277, 663–682.
- Lipari, G., and Szabo, A. (1982) *J. Am. Chem. Soc.* 104, 4559–4570.
- Lipari, G., and Szabo, A. (1982) *J. Am. Chem. Soc.* 104, 4546–4559.
- Clore, G. M., Szabo, A., Bax, A., Kay, L. E., Driscoll, P. C., and Gronenborn, A. M. (1990) *J. Am. Chem. Soc.* 112, 4989–4991.
- Mandel, A. M., Akke, M., and Palmer, A. G., III. (1995) *J. Mol. Biol.* 246, 144–163.
- Lin, H. Y., Wang, X.-F., Elinor, N.-E., Weinberg, R. A., and Lodish, H. F. (1992) *Cell* 68, 775–785.
- O'Connor-McCourt, M. D., Segarini, P., Grothe, S., Tsang, M. L.-S., and Weatherbee, J. A. (1995) *Annu. NY Acad. Sci.* 766, 300–302.
- Cornilescu, G., Marquardt, J. L., Ottiger, M., and Bax, A. (1998) *J. Am. Chem. Soc.* 120.
- Pepin, M. C., Beauchemin, M., Plamondon, J., and O'Connor-McCourt, M. D. (1996) *Biochem. Biophys. Res. Commun.* 220, 289–293.
- Qian, S. W., Burmester, J. K., Tsang, M. L.-S., Weatherbee, J. A., Hinck, A. P., Ohlsen, D. J., Sporn, M. B., and Roberts, A. (1996) *J. Biol. Chem.* 271, 30656–30662.
- Robertson, A. D. (2002) *Trends Biochem. Sci.* 27, 521–526.
- Forman-Kay, J. D. (1999) *Nat. Struct. Biol.* 6, 1086–1087.
- Ishima, R., and Torchia, D. A. (2000) *Nat. Struct. Biol.* 7, 740–743.

61. Szyperski, T., Luginbuhl, P., Otting, G., Guntert, P., and Wuthrich, K. (1993) *J. Biomol. NMR* 3, 151–164.
62. Loria, J. P., Rance, M., and Palmer, A. G., III. (1999) *J. Biomol. NMR* 15, 151–155.
63. Otting, G., Liepinsh, E., and Wuthrich, K. (1993) *Biochemistry* 32, 3571–3582.
64. Beeser, S. A., Oas, T. G., and Goldenberg, D. P. (1998) *J. Mol. Biol.* 284, 1581–1596.
65. Laskowski, R. A., MacArthur, M. W., Moss, D. S., and Thornton, J. M. (1993) *J. Appl. Crystallogr.* 26, 283–291.
66. Woessner, D. E. (1962) *J. Chem. Phys.* 37, 647–654.
67. Kabsch, W., and Sander, C. (1983) *Biopolymers* 22, 2577–637.
68. Koradi, R., Billeter, M., and Wuthrich, K. (1996) *J. Mol. Graph.* 14, 51–55.

BI034366A